







Quantitative analysis of free-electron dynamics in InSb by terahertz shockwave spectroscopy

Peter Fischer , Gabriel Fitzky , Davide Bossini , Alfred Leitenstorfer , and Ron Tenne ^{*}
Department of Physics and Center for Applied Photonics, University of Konstanz, D-78457 Konstanz, Germany

 (Received 11 April 2022; revised 5 October 2022; accepted 12 October 2022; published 7 November 2022)

The contribution of free electrons to the dielectric function is largely determined by their plasmonic resonance, a collective density oscillation. We studied this broadband and carrier-density-dependent response in the narrow-gap semiconductor InSb with THz shockwave spectroscopy. A synthesized waveform, with a steep onset followed by a short electric-field plateau, gives access to a multioctave spectrum of frequencies from 100 GHz up to the mid infrared. By measuring the entire spectral characteristics of the plasma, we analyze the dynamics of photogenerated free electrons for a wide range of excitation fluences. Thanks to this analysis, we were able to quantify the coefficients of both electron trapping and the Auger process from cryogenic to room temperature.

DOI: [10.1103/PhysRevB.106.205201](https://doi.org/10.1103/PhysRevB.106.205201)

I. INTRODUCTION

Optical-pump-optical-probe (OPOP) spectroscopy is arguably the most widespread approach to investigate the dynamics of magnetic, vibrational and electronic excitations in semiconductors (SCs) from the femtosecond to the nanosecond range [1,2]. While this method provides a wealth of information, in many cases it cannot capture the entire physical picture. An important example is the challenge of discerning the presence of excitons from that of free charge carriers in a SC, critical for understanding the dynamics of exciton formation and dissociation [3–6]. The lack of such quantitative and time-resolved information results in controversies with direct impact on, e.g., solar-cell technology [7].

Terahertz time-domain spectroscopy (THz-TDS) offers an alternative to OPOP in which charge carriers, photogenerated by an interband pump pulse, are probed with ultrashort electric transients in the terahertz (THz) range [8]. Notably, THz-TDS excels at disentangling the effects of bound and unbound charge carriers [3,9–11]. In SCs, the free-electron plasma exhibits a distinct longitudinal resonance which typically occurs in the mid-infrared (MIR) or far-infrared (FIR) spectral ranges. In addition, while spectrometer-based OPOP methods are insensitive to the spectral phase response, THz-TDS provides both the amplitude and phase information enabling a direct calculation of the dielectric function [8].

For narrow-gap SCs, instrumentation for OPOP becomes far more demanding, requiring a pulsed laser source and a sensitive detector in a challenging spectral regime. These materials, however, have significant technological applications, such as thermal imaging [12,13], and give rise to distinct and intriguing electronic phenomena. Due to very low electron-hole binding energy, they provide a test bed for quasi-free-electron phenomena, such as the Burstein-Moss effect [14,15] and the formation of massless fermions in topological insulators [16,17].

Indeed in InSb, one of the most prominent narrow-bandgap SCs, THz-TDS experiments provided valuable insights into the unique ultrafast electronics [18–20] and carrier dynamics [21,22]. However, since these experiments apply a narrow-band THz source, they are unable to capture the entire wide spectral fingerprint of the free-electron plasma and to, e.g., accurately determine its resonance frequency and damping. While many optical techniques obtain a signal that is proportional to the population of excited electrons, a precise measurement of the plasma frequency can determine the density of free electrons in an absolute manner. This capability is a prerequisite to study nonlinear electron dynamics, where monitoring a signal that is only proportional to the density is insufficient.

Still, wideband THz-TDS represents a highly nontrivial task. Typically, there is a trade-off between broadband and efficient detection. At the same time, generation of a wideband THz pulse is challenging as well [23,24] with successful demonstrations relying either on scanning the central wavelength [25,26] or generating a gas plasma with ultrashort pulses [27–29]. In general, access to the multi-THz regime comes at the price of strongly reduced sensitivity at few-THz frequencies whereas both are required for free-carrier plasma characterization in SCs. Exploiting the recently presented alternative wideband THz-generation method, namely the synthesis of a THz shockwave [30], circumvents these limitations. Photoactivating the reflection from a Ge wafer by means of sub-10 fs laser pulses induces a sharp step in a reflected few-THz transient. In the frequency domain, this effect manifests itself as a high-frequency tail which remains unhampered by phonon absorption in the generating medium [31] and results in continuous frequency coverage from approximately 100 GHz to beyond 40 THz.

Here, we introduce THz shockwave spectroscopy, extending THz-TDS to a wide frequency range in the FIR and MIR by employing a synthesized THz waveform with a steep onset as a probe pulse. The method is applied to capture the full spectral feature of the photogenerated electron plasma in InSb in order to study its unique decay dynamics. Although it is widely accepted that the recombination of electrons and

^{*}ron.tenne@uni-konstanz.de

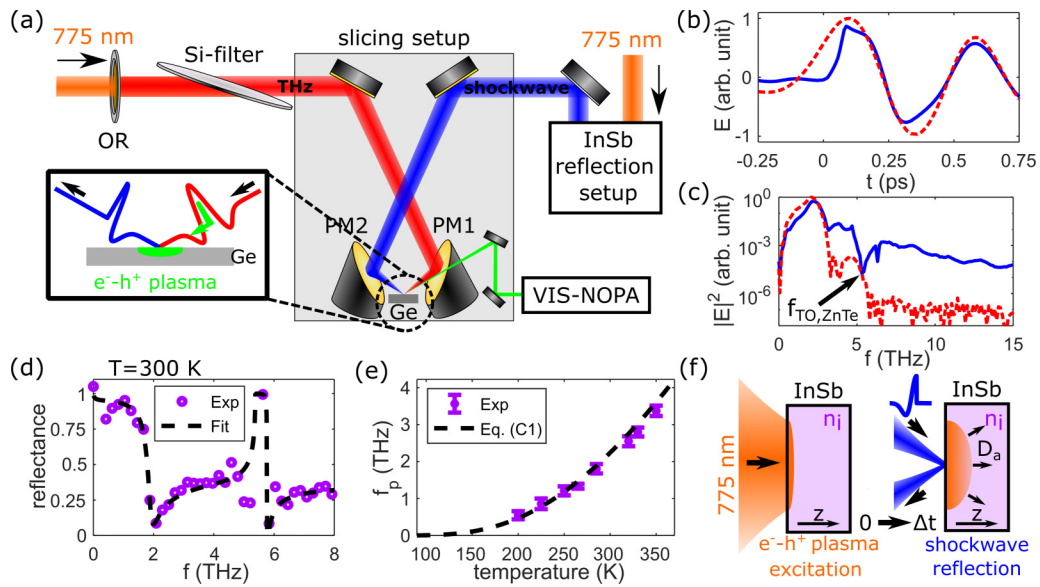


FIG. 1. (a) Schematic of slicing setup. A few-THz transient (red) is generated via optical rectification (OR) of a NIR ultrashort laser pulse (orange) and subsequently formed into a THz shockwave (blue) by a subcycle cut of the electric field (see inset). (b) Time traces of the electric field of the few-THz transient (dashed red) and the THz shockwave (solid blue) acquired via electro-optic sampling. (c) Intensity spectra of the few-THz transient (dashed red) and the THz shockwave (solid blue), as obtained by a Fourier transform. (d) Measurement (purple circles) and least-squares fit (dashed black) of intrinsic reflectance of InSb at room temperature. The feature around 5 THz arises from the contribution of optical phonons. (e) Temperature dependence of plasma frequency (purple dots). Error bars show 95% confidence intervals. Dashed black line represents parameter-free model (see Appendix C). (f) Cartoon of electron dynamics measurement. The NIR beam excites a dense electron-hole plasma at the surface which diffuses into the bulk of the sample. After a time interval Δt , the shockwave probes the diffused plasma.

holes in InSb is governed by the three-body Auger process, we find that Shockley-Read-Hall (SRH) recombination plays an equally important role in our sample. Moreover and surprisingly, the high Auger recombination rate increases even further if InSb is cooled from ambient conditions to cryogenic temperatures.

II. EXPERIMENTAL SETUP

To track the electron dynamics in narrow-band SCs, both a (i) broadband THz source and a (ii) broadband THz detection scheme are required. To meet the first requirement, we employ THz shockwave generation [30], a unique pulse-shaping technique that immensely broadens the spectral content of a few-cycle THz transient. The second prerequisite is fulfilled by performing electro-optic sampling (EOS) in a thin nonlinear crystal with an ultrashort near-infrared (NIR) sampling pulse.

Figure 1(a) schematically depicts the experimental setup: A few-cycle THz transient with a center frequency of 1.5 THz is generated via optical rectification (OR) of a 775-nm ultrashort NIR laser pulse in a 500- μm ZnTe crystal with $\langle 110 \rangle$ orientation [Fig. 1(b), red line]. The NIR pulse, featuring a 120 fs pulse duration and 3 mJ pulse energy, is produced by a hybrid system where a mode-locked Er:doped fiber laser seeds a Ti:sapphire amplifier [32]. Subsequently, the pump field is filtered by a Si wafer oriented at Brewster's angle with respect to the THz field.

Next, the THz transient enters the slicing setup in which the THz shockwave is synthesized [31]. The few-THz beam

(red) is focused by a parabolic mirror (PM1) on a Ge wafer, oriented at Brewster's angle to achieve near-zero reflection of the THz transient. A control pulse (green) with an ultrashort pulse duration of 7 fs full width at half maximum and a spectrum in the visible wavelength range (VIS) spatially overlaps the THz beam at the Ge surface. A dense electron-hole plasma, excited by the control pulse, effectively activates the reflection for the THz transient [inset in Fig. 1(a)]. Since the activation occurs on a much shorter time scale than the THz oscillation cycle, the transient is abruptly sliced into two parts. The trailing portion of the waveform is reflected, yielding a sharp onset of the electric field [Fig. 1(b), blue line]. Thus, the reflected THz field, termed here a THz shockwave, forms an optical analog to acoustic shockwaves. At the focal plane of a parabolic mirror (30-mm focal length), the peak electric field of the shockwave waveform is 90 kV/cm, comparable with gas-plasma based sources that achieve a broadband THz spectrum [19].

The intensity spectra of the few-THz (red) and THz shockwave (blue) pulses are depicted in Fig. 1(c). Note that the sharp temporal feature of the shockwave translates into a remarkable broadening of the spectral content compared to the original few-THz transient. The narrow dip around 5.5 THz results from an absorption due to the transverse optical phonon in the ZnTe detector crystal. Due to the low signal-to-noise ratio (SNR), this spectral region is not exploited for the following data analysis.

To demonstrate the absolute quantitative nature of shockwave spectroscopy, we first measure the intrinsic reflectance of an undoped bulk InSb sample ($\langle 100 \rangle$ orientation) at room

temperature. To obtain the sample's reflectance $\mathcal{R}(f)$, we divide the THz shockwave spectral intensity reflected from bulk InSb ($I_{\text{InSb}}(f)$) with that reflected from an evaporated Au film ($I_{\text{Au}}(f)$), with close to unity reflectance in the FIR and MIR:

$$\mathcal{R}(f) = I_{\text{InSb}}(f)/I_{\text{Au}}(f). \quad (1)$$

The result is depicted in Fig. 1(d) by purple circles. While the reflectance is close to unity for very low frequencies, it exhibits a deep minimum at about 2 THz. This feature marks the resonance frequency of the intrinsic plasmon f_p , i.e., the collective oscillation of the intrinsic electron density. In this spectral range, the reflectance can be readily calculated by combining the Drude-Lorentz model for the dielectric function with the Fresnel formula (see Appendixes A and B). The resulting free-electron plasma frequency is

$$f_p = \frac{1}{2\pi} \sqrt{\frac{n_i e^2}{\epsilon_0 \epsilon_\infty m_{\text{opt}}^*}}, \quad (2)$$

where the only variables are the intrinsic carrier density n_i and the optical effective mass m_{opt}^* (see Appendix A). The elementary charge is denoted by e and the vacuum permittivity by ϵ_0 . In InSb, the high-frequency dielectric constant ϵ_∞ amounts to 15.68 [33]. We note that, strictly speaking, the mass entering the expression in Eq. (2) is the electron-hole reduced mass. However, in InSb, the heavy-hole mass is much larger than that of the electron in the conduction band. Hence, the reduced mass is well approximated by the effective mass of the electron.

The dashed black line in Fig. 1(d) depicts a least-squares fit of the Drude-Lorentz reflectance from which we extract $f_p = (2.04 \pm 0.03)$ THz. Using Eq. (2), we determine $n_i = (1.65 \pm 0.02) \times 10^{16} \text{ cm}^{-3}$, in good agreement with the literature [33] (see Appendix B for an in-depth analysis). Similarly, we determine f_p for a range of temperatures from 200 to 350 K [purple dots in Fig. 1(e)]. The experimental values are in excellent agreement with a parameter-free model (dashed black line, see Appendix C). Note that this accurate estimate of the absolute density of free electrons emerges from the broadband nature of the measurement. This unique capability shows the potential of THz shockwave spectroscopy to study nonlinear electron dynamics by following the absolute density of charges with a high temporal resolution.

III. THz SHOCKWAVE SPECTROSCOPY OF PHOTOEXCITED InSb

To demonstrate this potential, we measure the THz-shockwave reflection following free-carrier generation by a short NIR laser pulse (120 fs, 775 nm). The principle is sketched in Fig. 1(f): Due to the high absorption coefficient of InSb at 775 nm ($\alpha = 1.1 \times 10^5 \text{ cm}^{-1}$), the NIR pulse creates a dense excess charge-carrier plasma close to the surface of the sample. Subsequently, the concentration gradient drives diffusion into the depth of the sample while recombination reduces the total number of charge carriers. The time delay Δt between excitation and probe reflection determines the extent by which these two processes have progressed. For the experiments presented here, a time delay of $\Delta t = 300$ ps

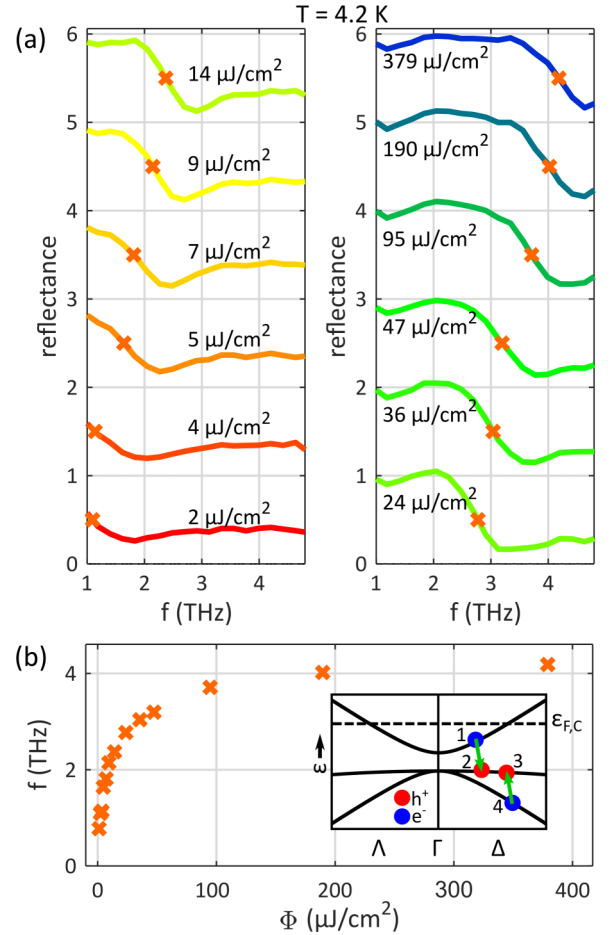


FIG. 2. (a) Excess charge carrier plasma reflectance of InSb at $T = 4.2$ K, as measured for various excitation fluences. (b) Evolution of plasma-edge frequency with excitation fluence. Inset depicts band-structure representation of one of the dominant Auger recombination channels under degeneracy.

was selected. Under this condition, the shockwave encounters an already widespread, but still inhomogeneously distributed electron plasma.

A series of reflectance measurements of InSb at $T = 4.2$ K for various excitation fluences Φ is depicted in Fig. 2(a). To highlight the effect of the excitation fluence, the reflection spectra in Fig. 2(a) are presented only in the 1–5 THz range, whereas a broader range (0–15 THz) of the same dataset is given in Fig. 7 of Appendix D. Unlike the spectrum shown Fig. 1(d), at this temperature, virtually no charge carriers are excited thermally so that for $\Phi = 0$ the reflectance is nearly a constant. Conversely, for $\Phi \neq 0$, the reflectance is governed by the excess-carrier plasma. As Φ increases, the entire plasma characteristic blueshifts, most noticeable in the variation of the sharp edge of high reflectance. To qualitatively examine this trend, Fig. 2(b) presents the plasma-edge frequency, defined as the lowest frequency at which the reflectance drops to 0.5 [orange crosses in Fig. 2(a)] vs Φ . A nonlinear saturating dependence emerges, reflecting a sharp increase in the recombination rate with a growing excitation intensity.

In the following, our objective is to identify and reproduce the physics underlying the experimental spectroscopic data. We thus simulate the recombination and diffusion of free carriers in order to fit the measured reflection spectra. Note that the entire evolution of these processes, starting at the time of excitation ($t = 0$), determines the depth profile of the free-carrier density and, as a result, the broadband shape of the THz reflection spectra. Therefore, despite the fact that the pump-probe delay is kept constant in our experiments, we obtain information about electronic processes that occur within the entire interval up to the arrival of the THz shockwave probe at $t = 300$ ps.

It is well known that in narrowband semiconductors Auger recombination, a nonlinear process, dominates carrier recombination [34]. This fundamental process has significant technological consequences, e.g., for the efficiency of light-emitting diodes [35]. To understand the density dependence of its rate, we take a closer look at one of its dominant channels [inset of Fig. 2(b)]: An electron in the conduction band recombines with a hole in the heavy-hole valence band while a second heavy hole is resonantly excited to the light-hole valence band. The rate of recombination, R , depends on the occupation probability of the participating states and therefore on the excess charge carrier density n . For very low n , the recombination rate possesses the well-known $R \propto n^3$ dependence [21]. However, in InSb, already for moderate electron densities, the conduction-band Fermi energy $\varepsilon_{F,C}$ surpasses the band edge considerably. At this point, degeneracy develops in the Γ -valley of the conduction band, altering the dependence of the recombination rate on the excess carrier density to $R \propto n^2$ [36]. The rate of the additional pathways for Auger recombination presents the same scaling with n .

To quantitatively analyze the recombination dynamics, we numerically simulate the evolution of the excess carrier density $n(z, t)$ with the rate equation

$$\frac{\partial n(z, t)}{\partial t} - D_a \frac{\partial^2 n(z, t)}{\partial z^2} = -R(z, t), \quad (3)$$

where z denotes the depth with respect to the sample surface. Here, due to the much larger spot size of the excitation pulse on the sample surface compared to the THz shockwave [Fig. 1(f)], we neglect the fluence variation across the THz beam. The ambipolar diffusion coefficient D_a describes the coupled diffusion of electrons and holes. It is determined from fitting the low-fluence data (see Appendixes E and F).

Considering a short excitation pulse, the initial condition for Eq. (3) follows

$$n(z, 0) \propto \Phi \times e^{-\alpha z}. \quad (4)$$

In a first attempt to model the charge-carrier dynamics, we insert $R(z, t) = \gamma_2 \times n(z, t)^2$ in Eq. (3) in which γ_2 is the Auger recombination coefficient. Employing a transfer-matrix approach for the simulated density profiles, we calculate the THz reflection spectra (see Appendix E). To estimate the model parameters, we fit the simulated data to the experimental results according to a least-mean-squares criterion. The computational details of the fitting procedure are reported in Appendix E.

Figure 3 depicts the extracted value of γ_2 vs Φ for a temperature of $T = 4.2$ K alongside an example for the numerical

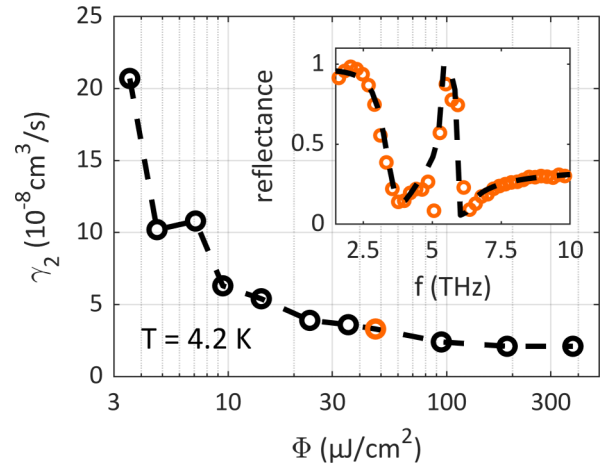


FIG. 3. Auger recombination coefficient, extracted from least-square fits of excess charge carrier reflectance, over excitation fluence. Measurements were acquired at $T = 4.2$ K. Orange circle at $47.3 \mu\text{J}/\text{cm}^2$ corresponds to reflectance depicted in the inset, in which the black dashed line represents the fit.

fit. Surprisingly, even though γ_2 should be independent of the excitation fluence, we observe an order of magnitude difference between its estimates for low and high fluences. While at high fluences γ_2 asymptotically approaches a constant value, it strongly diverges at low fluences. This overestimate for low electron densities indicates the presence of an additional recombination mechanism with a weaker dependence on the electron density, that was not contained in the model above. This finding is rather surprising as it shows that the Auger mechanism, often reported as the only significant recombination process in narrow-gap InSb, is insufficient to capture the measured dynamics here [21]. We therefore consider an additional mechanism that reduces the free electron density—electron trapping in defect sites, also known as SRH recombination. Since SRH leads to a linear recombination rate, we expand the model to include such a term, so that

$$R(z, t) = \gamma_2 n(z, t)^2 + \gamma_1 n(z, t), \quad (5)$$

where γ_1 is the linear recombination coefficient. In the following, we show that unlike a model that includes only Auger processes, the extended theory can fit the entire experimental dataset with constant parameter values.

To explore the quality of the fit in Figs. 4(a)–4(c), we depict the mean-squared error (MSE) (see Appendix E) indicating the agreement between the simulation and the measured data for three different pump fluences. For each individual measurement, a significant portion of the parameter space accurately fits the experimental data characterized by a nearly minimal MSE (blue areas). As expected from the model, trapping (γ_1) is the most probable recombination channel for low Φ (horizontal orientation of MSE minimum) whereas for high pump fluences, Auger scattering becomes the dominant relaxation mechanism (vertical orientation of MSE minimum). To find a parameter combination that reproduces the entire data set, we minimize the MSE summed over all fluences. The result [Fig. 4(d)] presents a well-defined parameter combination that optimally fits the data: $\gamma_1 = (3.2 \pm 0.1) \times 10^9 \text{ 1/s}$

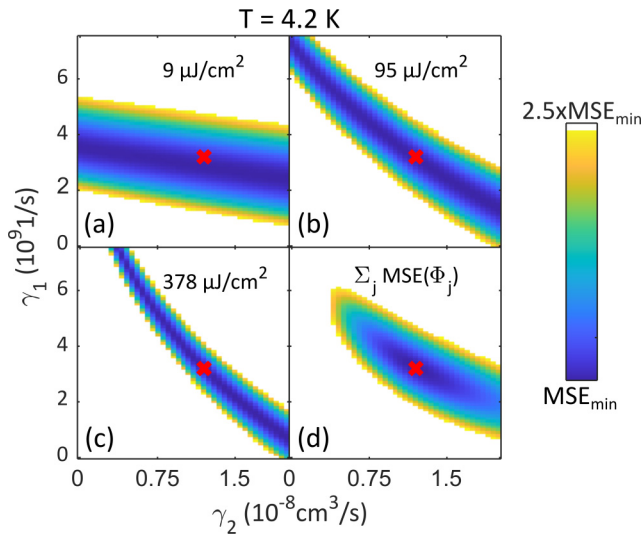


FIG. 4. Mean-square error (MSE) maps in two-dimensional parameter space of linear (γ_1) and Auger (γ_2) recombination coefficients. (a) to (c): Examples of 3 out of 12 measurements acquired at $T = 4.2$ K for different excitation fluences, as indicated in each panel. (d) Sum of all 12 MSE maps. Red crosses in each panel indicate the parameter combination that simultaneously provides good estimates for all measured fluences.

and $\gamma_2 = (1.2 \pm 0.1) \times 10^{-8} \text{ cm}^3/\text{s}$. We indicate these fitted values with a red cross in all panels to emphasize the quality of this choice for all excitation fluences (see Appendix G). This analysis confirms that the minimal extension (one additional parameter) of the previously employed electron dynamics model is sufficient to recreate the entire measured data set. Moreover, by analyzing the spectral phase of the reflection, we demonstrate that the same parameters simultaneously fit both the amplitude and phase of the reflection spectra (see Figs. 6 and 8).

We emphasize here that unlike most pump-probe approaches, the analysis procedure introduced here obtains an absolute, rather than proportional, estimate of the electron density profile (see Fig. 9). For example, commonly applied interband transient transmission methods can provide a time-resolved signal that is only proportional to the density of charge carriers. In contrast, the dependence of the plasma spectral position and shape on the carrier density profile enables its reconstruction in absolute terms. In combination with the modeling procedure, this feature renders THz shockwave spectroscopy highly suitable for studying free-carrier recombination and transport.

Finally, γ_1 and γ_2 are studied at five different sample temperatures between 4.2 and 200 K exploiting the procedure outlined above. As a result of a slower diffusion rates at higher temperatures, the plasma spectral features further broaden with increased temperature (see Fig. 9). The extension of spectral features over the range of 0.1–10 THz (in comparison with a 0.1–4.5 THz range at 4.2 K) emphasizes the advantage provided by the large spectral bandwidth of the THz shockwave. Figure 5 presents the extracted values for γ_1 and γ_2 vs temperature and their asymptotic standard errors. The values for γ_1 (blue) show considerable (up to

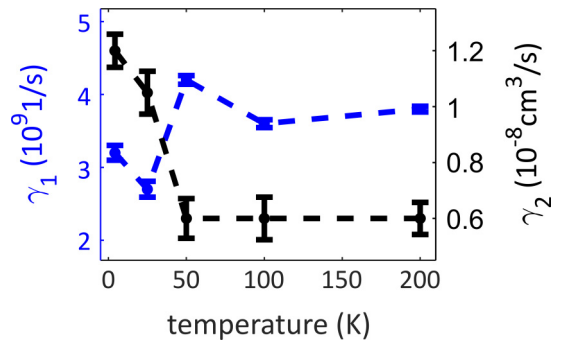


FIG. 5. Linear (γ_1 , blue) and Auger (γ_2 , black) recombination coefficient vs temperature. For each temperature, we extract the parameter combination that simultaneously provides good estimates for measurements at 12 different fluences. Error bars represent asymptotic standard error.

60 %), yet seemingly random, deviations from one another. The lack of a clear temperature dependence, combined with the linear nature of this term, supports its interpretation as an electron trapping rate. In contrast, a clear temperature trend emerges for the Auger recombination coefficient. While at high temperatures ($T \geq 50$ K), the value is constant around $\gamma_2 = 6 \times 10^{-9} \text{ cm}^3/\text{s}$, it abruptly increases below $T = 50$ K. At 4.2 K, the rate is almost twice its room-temperature value. We note that the extracted rate of this three-body process is so high as to be comparable to the rate of two-body radiative recombination in direct wide-gap semiconductors. For example, in GaAs the radiative recombination coefficient is $1.8 \times 10^{-8} \text{ cm}^3/\text{s}$ at 90 K [37], i.e., only three times as large as the Auger coefficient found here.

At room temperature, our estimate agrees well with some previous results [36] and is in the same order of magnitude as others [38]. These results have also found use in several studies of electron dynamics in InSb that produced good agreement with theoretical models [39,40]. However, despite differing sources and qualities of samples, including commercially available wafers and thin films grown by molecular beam epitaxy, none of these studies required the addition of electron trapping in the interpretation of their results. One explanation for this inconsistency is that the high sensitivity of our method, delivered by its broadband character, enables accurate determination of the recombination dynamics even at low electron densities revealing the additional SRH recombination mechanism.

IV. CONCLUSIONS

This work demonstrates the concept of THz shockwave spectroscopy. Applying a source of coherent THz radiation, namely a THz shockwave, enables performing THz-TDS on a large span of frequencies in the FIR (0.2–15 THz). By fully capturing the plasma resonance feature of free electrons in InSb, we determine the absolute density profile of free electrons. Applied here to study nonlinear electron dynamics in InSb, THz shockwave spectroscopy could be applied to quantitatively study electronic transport and dynamics in various semiconductors. It also holds great potential for testing practical optoelectronic devices. For example, a combination

of the current method with VIS or NIR pump-probe spectroscopy would allow us to simultaneously track free and bound electrons in Perovskite solar cells where both species and their interplay determine performances [5,11].

ACKNOWLEDGMENTS

Funded by the Deutsche Forschungsgemeinschaft (DFG) – Project-ID 425217212 – SFB 1432. This work was supported by the Deutsche Forschungsgemeinschaft through DFG programme BO 5074/1-1, and BO 5074/2-1. R.T. acknowledges support by the Minerva foundation.

P.F. and G.F. contributed equally to this work.

APPENDIX A: KANE MODEL AND THE ELECTRON EFFECTIVE OPTICAL MASS IN A NONPARABOLIC BAND

InSb is a direct III-V semiconductor with a comparatively low fundamental band gap of $\varepsilon_g = 180$ meV at room temperature. As a consequence, the electron effective mass in the center of the Brillouin zone ($\mathbf{k}_0 = 0$, \mathbf{k} is the electron wave vector) is extremely small and amounts to $m_0^* = 0.0118m_0$. In the vicinity of \mathbf{k}_0 (Γ valley) the conduction band is isotropic to a good approximation but it exhibits a strong nonparabolicity. The dispersion relation can be expressed by the four-band Kane model [41] in first-order nonparabolic approximation as [42]

$$\varepsilon_c(k) = -\frac{\varepsilon_g}{2} + \left[\left(\frac{\varepsilon_g}{2} \right)^2 + \varepsilon_g \frac{\hbar^2 |\mathbf{k}|^2}{2m_0^*} \right]^{1/2}. \quad (\text{A1})$$

Due to the nonparabolicity, the Γ -valley effective mass depends on the electron energy ε_c and takes the form

$$m^*(\varepsilon_c) = m_0^* \left(1 + \frac{2\varepsilon_c}{\varepsilon_g} \right). \quad (\text{A2})$$

Since the small effective mass translates to a low density of states at the bottom of the conduction band, degeneracy occurs already for low excess electron densities. In such a case, the Sommerfeld model for the conductivity of a degenerate free electron gas suggests that in reciprocal space only the carriers in the thermally broadened region close to the Fermi energy (ε_F) contribute to transport. Therefore, the effective mass observed in optical experiments is a mean value of the effective masses only of these carriers. In the approximation of the first-order nonparabolicity [Eq. (A2)], it can be calculated via [42]

$$m_{\text{opt}}^*(\varepsilon_F) = m_0^* \frac{{}_0L_{0}^{3/2}(\varepsilon_F)}{{}_0L_{-1}^{3/2}(\varepsilon_F)}, \quad (\text{A3})$$

where

$${}_nL_k^m = \int_0^\infty \left(-\frac{\partial f_0}{\partial z} \right) z^n (z + \beta z^2)^m (1 + \beta z)^k dz, \quad (\text{A4})$$

are the generalized Fermi-Dirac integrals. Here, f_0 is the Fermi-Dirac distribution. In addition, $z = \varepsilon_c(k)/k_B T$, $\eta = \varepsilon_F/k_B T$ and $\beta = k_B T/\varepsilon_g$, where k_B is the Boltzmann constant.

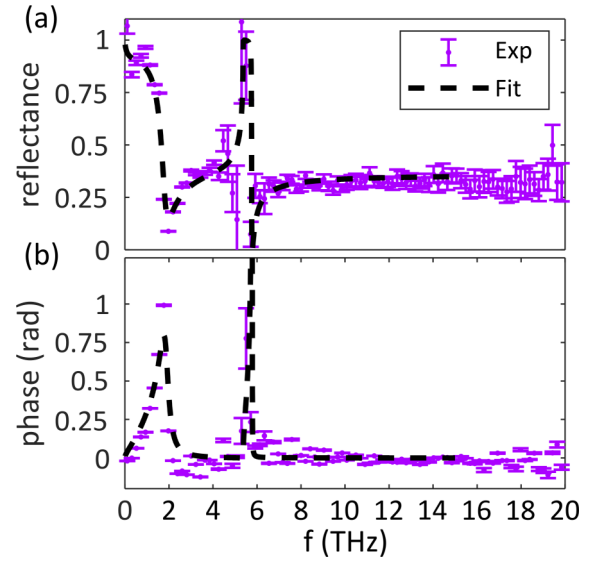


FIG. 6. (a) Measurement of intrinsic reflectance of InSb at room temperature (purple dots) and least-squares fit of Drude-Lorentz model (dashed black). Error bars represent standard deviations. (b) Reflection spectral phase shift analyzed from the same dataset.

APPENDIX B: DIELECTRIC FUNCTION UNDER THE DRUDE-LORENTZ MODEL

The light-matter interaction of InSb in the low-THz frequency range can be described by the Drude-Lorentz model for the dielectric function [43]

$$\varepsilon(f) = \varepsilon_\infty \left(1 - \frac{f_p^2}{f^2 - \frac{if\gamma_d}{2\pi}} + \frac{f_{\text{LO}}^2 - f_{\text{TO}}^2}{f_{\text{TO}}^2 - f^2} \right). \quad (\text{B1})$$

Here, ε_∞ is the high-frequency dielectric constant, γ_d the damping constant and $f_{\text{TO/LO}}$ are the transverse/longitudinal resonance frequencies of the zone-center optical phonons, respectively. In InSb, $f_{\text{TO}} = 5.37$ THz and $f_{\text{LO}} = 5.71$ THz [43]. The plasma frequency f_p may be expressed as

$$f_p = \frac{1}{2\pi} \sqrt{\frac{n_e e^2}{\varepsilon_0 \varepsilon_\infty m_{\text{opt}}^*(n_e)}}, \quad (\text{B2})$$

with respect to the electron density in the conduction band n_e . Note that since m_{opt}^* depends on ε_F , it is itself a function of n_e .

Furthermore, the frequency-dependent penetration depth $d(f)$ can be calculated from the dielectric function as the reciprocal value of the absorption coefficient $\alpha(f)$ via [43]

$$d(f) = \alpha(f)^{-1} = \left(\frac{2\pi f}{c} \times \text{Im}(\sqrt{\varepsilon(f)}) \right)^{-1}, \quad (\text{B3})$$

where $\text{Im}(\dots)$ denotes the imaginary part and c the speed of light.

Inserting Eq. (B1) into the Fresnel equations, one obtains the complex frequency-dependent reflection coefficient $r = \sqrt{\mathcal{R}} \times \exp(i\Phi_r)$ where \mathcal{R} and Φ_r denote the reflectance amplitude and phase, respectively. Figures 6(a) and 6(b) depict \mathcal{R} as well as Φ_r for a reflection spectrum measured for intrinsic InSb at room temperature. The experimental data (purple

dots) fit well to the Fresnel equation (dashed black lines). We note that only \mathcal{R} is considered in the fitting procedure. The phase data are used to validate the goodness of our fit. An experimental issue tackled here is the shift of the time origin in different measurements (e.g., reflection off Au and InSb). This aspect is compensated for by fitting the general linear phase trend in the spectrum of Φ_r and subtracting it.

The error bars for the experimental data represent the standard deviation obtained from sequential repetition of the transient measurement (see also Appendix H). In the frequency region around 5.5 THz, the SNR is drastically reduced due to optical phonon resonances in the ZnTe detector crystal. However, especially at low frequencies, a very high SNR is achieved (> 40 for $f \leq 4$ THz for a 20-min measurement averaging 3000 transients). At higher frequencies, the SNR continuously decreases (corresponding to an increase of the error bars) due to the decline of the spectral amplitude of the source. In addition, our EOS setup employs a 30- μm -thick ZnTe crystal optimized for sensitive detection in the frequency range up to 10 THz. Still, it features a sensitivity minimum (due to phase mismatch) only at a frequency as high as 30 THz.

APPENDIX C: A PARAMETER-FREE MODEL FOR THE TEMPERATURE DEPENDENCE OF THE PLASMA FREQUENCY

In InSb, the temperature dependence of the intrinsic carrier density can be calculated according to [33]:

$$n_i(T) = 5.76 \times 10^{14} \frac{\text{cm}^{-3}}{\text{K}^{3/2}} \times T^{3/2} \exp\left(-\frac{0.26 \text{ eV}}{2k_B T}\right). \quad (\text{C1})$$

By inserting Eq. (C1) into Eq. (B2), one receives the temperature dependence of the plasma frequency of intrinsic InSb, depicted as dashed black line in Fig. 1(e) of the main text.

APPENDIX D: FULL RANGE PRESENTATION OF THE FLUENCE-DEPENDENT REFLECTION SPECTRA

Figure 7 shows the same dataset presented in Fig. 2 of the main text but extended to a much broader spectral range. Note that the reflection feature appearing around 5.5 THz is associated with the response of the phonons in InSb and is therefore not significantly modified by varying the excitation fluence.

APPENDIX E: THE TRANSFER-MATRIX METHOD

The transfer-matrix method [44] presents an exact approach to solve Maxwell's equation for a stratified medium, i.e., a medium consisting of multiple layers with infinite lateral dimensions. Given a simulated carrier-density profile ($n(z)$), yielding a local plasma frequency ($f_p(z)$), we evaluate the complex reflection coefficient $r_{\text{sim}}(f)$ by inserting the transfer matrix

$$M = \prod_{l_z} \begin{bmatrix} \cos(k_{l_z}(f)dz) & 1/k_{l_z}(f) \times \sin(k_{l_z}(f)dz) \\ k_{l_z}(f) \times \sin(k_{l_z}(f)dz) & \cos(k_{l_z}(f)dz) \end{bmatrix}, \quad (\text{E1})$$

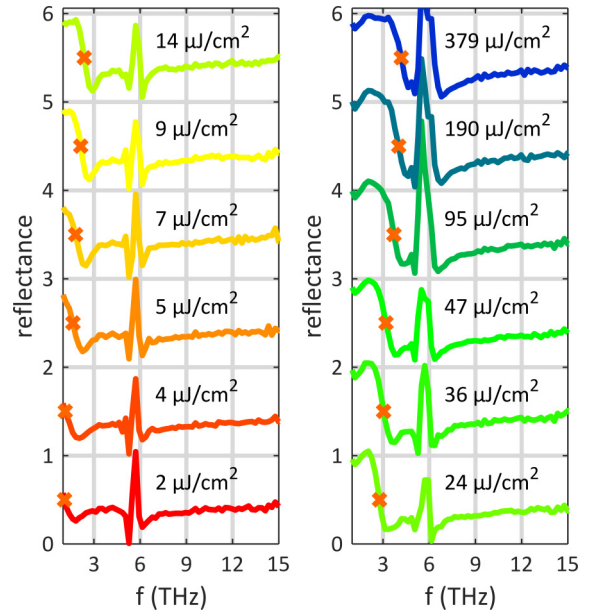


FIG. 7. Excess charge carrier plasma reflectance of InSb at $T = 4.2$ K, as measured for various excitation fluences

into

$$r_{\text{sim}}(f) = \frac{ik_0(f)M_{11} - k_0(f)k_{\text{intr}}(f)M_{12} - M_{21} - ik_{\text{intr}}(f)M_{22}}{ik_0(f)M_{11} - k_0(f)k_{\text{intr}}(f)M_{12} - M_{21} + ik_{\text{intr}}(f)M_{22}}, \quad (\text{E2})$$

where the wave vector of the incident THz field in each layer is calculated by $k_{l_z}(f) = \sqrt{\epsilon_{l_z}(f)}2\pi f/c$. In addition, $k_0(f)$ is the wave vector in the topmost medium, i.e., free space in this case. The wave vector in the medium at the bottom, where the carrier density is intrinsic, is denoted by $k_{\text{intr}}(f)$. Each point l_z of the simulated density profiles (thickness dz), is assigned with the carrier density $n(l_z \times dz, t)$. The dielectric function of each layer is again given by Eq. (B1). As a last step, the reflectance is obtained by $\mathcal{R}_{\text{sim}} = |r_{\text{sim}}|^2$.

To qualitatively compare our simulation results to the experimental reflectance spectra, as shown in Fig. 4 of the main text, the deviation for each simulated reflection spectrum is calculated by the MSE

$$\text{MSE} = \frac{1}{N} \sum_{i=1}^N (\mathcal{R}_{\text{exp}}(f_i) - \mathcal{R}_{\text{sim}}(f_i))^2, \quad (\text{E3})$$

where $\mathcal{R}_{\text{exp}}(f_i)$ denotes the measured reflectance and N the total number of data points in the discrete frequency spectrum. In all the analysis discussed and presented in this work, the MSE is summed within a range from 1 to 10 THz excluding a 0.8 THz wide spectral window centered at the ZnTe phonon frequency, 5.5 THz.

Similar to Fig. 6, Fig. 8 depicts not only the reflectance \mathcal{R} [(a) to (c)] but also the corresponding spectral phase Φ_r [(d) to (f)] of the reflection coefficient for a measurement of InSb at 4.2 K under three different excitation fluences (indicated in the top figures). We emphasize here the consistency of the

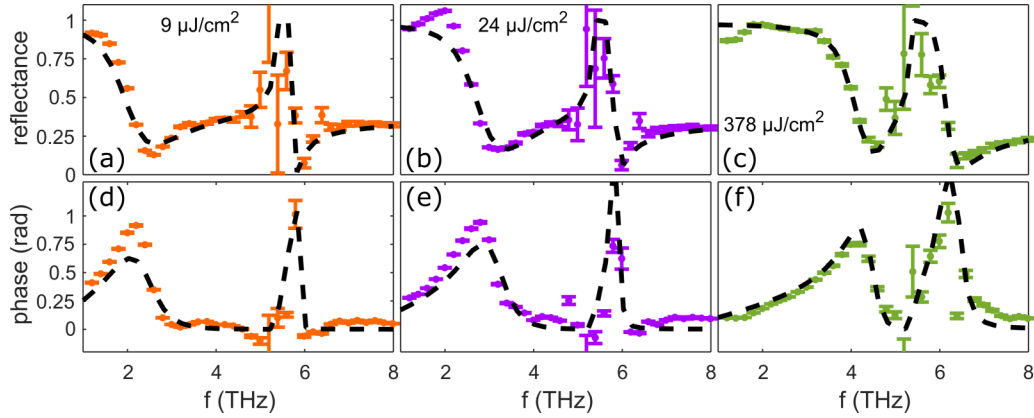


FIG. 8. (a)–(c) present experimental (colored dots) and best-fit model (dashed black) reflectance spectra of InSb at 4.2 K excited with the three different fluences indicated in the figures. Error bars result from averaging. (d) to (f) present corresponding phases extracted from top figures.

fitting quality for different excitation fluences both for the reflectance amplitude and spectral phase data.

APPENDIX F: THE AMBIPOLAR DIFFUSION COEFFICIENT

Beyond the recombination coefficient, another relevant parameter for the electron dynamics simulations used in this work is the ambipolar diffusion coefficient, D_a . This coefficient is expected to strongly depend on temperature and to some degree also on the charge-carrier densities [45]. For InSb, experimental data and theoretical modeling for these dependences are rather scarce. However, the plasma response spectra measured in this work are only weakly sensitive to the value of D_a . The following discussion explains the reasoning for this fact (that can be confirmed in simulations) and provides the protocol applied here to estimate D_a for different measurement temperatures.

As an approximation, let us consider an approximate step-like charge density profile in the axial direction (into the sample). We assume that the profile roughly preserves its steplike shape while it penetrates deeper into the InSb film by diffusion. Neglecting diffusion in the x - y plane as well as recombination, the conservation of total particle number im-

plies that the product of carrier density and penetration depth is constant ($n_e \times l_D = \text{const}$). As a result, n_e is proportional to l_D^{-1} . Since l_D is roughly proportional to the square root of D_a ($l_D \propto \sqrt{D_a \times \tau}$), the density follows $n_e \propto D_a^{-1/2}$. The plasma frequency, in turn, depends on the square root of n_e and therefore $f_p \propto D_a^{-1/4}$. In this simplified picture, a doubling of D_a leads to a decrease of f_p by approximately 15%. In fact, applying the electron dynamics simulations we observe a decrease of the plasma edge frequency by approximately 10% only after increasing D_a by an entire order of magnitude.

To further verify the weak dependence of our results on D_a , we carry out the electron dynamics simulation process [Eq. (3)–(5) and Appendix E] with γ_2 and D_a as the two model parameters. The results, presented in Fig. 9(a), provide an example of the MSE maps for four different temperatures at the same excitation fluence of $\Phi = 24 \mu\text{J}/\text{cm}^2$. The vertically elongated MSE minima (blue areas) indicate that while the fit to the data is very sensitive to the recombination dynamics, it is nearly insensitive to the diffusion process.

As a result of the discussion above, our simulations include the diffusion coefficient in the following phenomenological manner. In order to perform the simulation only in a two-dimensional parameter space $\{\gamma_2, \gamma_1\}$, as presented in Fig. 4 of the main paper, we estimate D_a on the basis of the

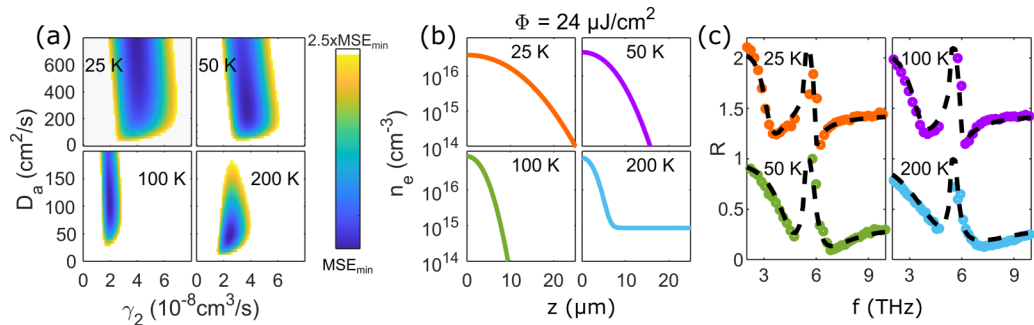


FIG. 9. (a) MSE maps in two-dimensional parameter space of the Auger coefficient (γ_2) and ambipolar diffusion coefficient (D_a) at four different temperatures. White-colored areas indicate $\text{MSE} \geq 2.5 \times \text{MSE}_{\min}$. (b) Density profiles simulated with the D_a listed in Table I and corresponding γ_2 at MSE_{\min} ($\gamma_2(25 \text{ K}) = 3.9 \times 10^{-8} \text{ cm}^3/\text{s}$, $\gamma_2(50 \text{ K}) = 3.7 \times 10^{-8} \text{ cm}^3/\text{s}$, $\gamma_2(100 \text{ K}) = 2.0 \times 10^{-8} \text{ cm}^3/\text{s}$, $\gamma_2(200 \text{ K}) = 2.5 \times 10^{-8} \text{ cm}^3/\text{s}$). (c) Corresponding reflectance spectra. The dashed black line represents the model [Eq. (E2)] and colored circles experimental data.

TABLE I. Estimates of temperature-dependent ambipolar diffusion coefficient on basis of simulations in two-dimensional parameter space $\{\gamma_2, D_a\}$.

| T | 4.2 K | 25 K | 50 K | 100 K | 200 K |
|-------|------------------------|------------------------|------------------------|------------------------|-----------------------|
| D_a | 800 cm ² /s | 800 cm ² /s | 300 cm ² /s | 100 cm ² /s | 60 cm ² /s |

simulations in $\{\gamma_2, D_a\}$ [Fig. 9(a)] for relatively high excitation fluences. The results are listed in Table I. It is worth noting that at low temperatures, D_a increases considerably. This finding may be explained by the direct mobility dependence of diffusion: since acoustic and polar-optical scattering are drastically reduced at low temperatures, the mobility of free carriers and consequently also D_a increases.

Furthermore, for lower temperatures the blue-colored areas span over a much larger range of D_a (note the different y axis scaling at 25 and 50 K compared the cases of 100 and 200 K). This indicates that our method becomes even less sensitive to D_a at cryogenic temperatures. In order to explain this observation, Fig. 9(b) depicts the density profiles simulated with the D_a values listed in Table I and the corresponding γ_2 of the best fit. As expected, for lower temperatures the profile extends further into the z direction. Conversely, this finding means that for high temperatures the charge carriers remain concentrated close to the sample surface. In addition, at 200 K a significant intrinsic carrier density emerges, visible as a constant offset in the density profile.

Now, to explain the shape of the MSE on a qualitative level, we need to estimate the penetration depth $d(f)$ of the THz radiation in the frequency range of the characteristic plasma reflectance. For this purpose, we insert the Drude-Lorentz result for a homogeneously distributed plasma [Eq. (E2)] into Eq. (E3). For the charge-carrier density, we insert $n_e = 6 \times 10^{16} \text{ cm}^{-3}$ which roughly corresponds to the density close the sample surface in Fig. 9(b). We calculate the penetration depth for a frequency of $f = 3 \text{ THz}$ and receive a value of $d \approx 6 \mu\text{m}$. Compared to the scale of z in Fig. 9(b), we conclude that at high temperatures the THz can indeed probe the entire high-density portion of the carrier-density profile, i.e., its steep decrease. However, the low-temperature case

is different. Here, the THz radiation does not penetrate far enough during the reflection to probe the complete decay of the profile. Therefore, the effects of diffusion remain partially undetected, resulting in the reduced sensitivity of reflectance on the value of D_a we observe.

To support this argument, the corresponding reflectance spectra are plotted in Fig. 9(c). The dashed black lines represent the reflectance spectra that were evaluated with the transfer-matrix method from the density profiles in Fig. 9(b). The colored circles depict the experimental data. At 25 K, the steepness of the plasma edge, best discernable in the frequency range between 2 and 4 THz, is comparable to that of the Drude reflectance of a homogeneously distributed intrinsic plasma [Fig. 1(d)]. This finding confirms that, in this case, the THz indeed experiences a rather homogeneous plasma and does not probe the high-gradient portion of the profile. However, this feature becomes less sharp (Drude-like) at higher temperatures, indicating an inhomogeneous carrier distribution.

APPENDIX G: COMPLETE MEASUREMENT SERIES

In Fig. 4 of the main paper, we show three out of 12 MSE maps for the estimation of the Auger (γ_2) and linear (γ_1) recombination coefficients at 4.2 K as an example. In Fig. 10, the MSE maps of all 12 measurements are depicted for completeness. For each excitation fluence Φ (indicated at the bottom of each panel), a range of parameter values fits the experimental data well (blue-colored areas). When Φ is increased, the blue-colored area rotates continuously towards a vertical orientation, indicating a decreasing sensitivity for γ_1 and an increasing one for γ_2 . The red crosses denote the parameter set γ_1 and γ_2 which minimizes the total MSE for all Φ together.

APPENDIX H: ELECTRO-OPTIC SAMPLING

After its generation, the shockwave is guided through a reflection-geometry setup in which the sample is placed within a liquid-helium flow cryostat.

Subsequently, the experimental time-domain signal is detected via free-space EOS: The THz signal is superimposed

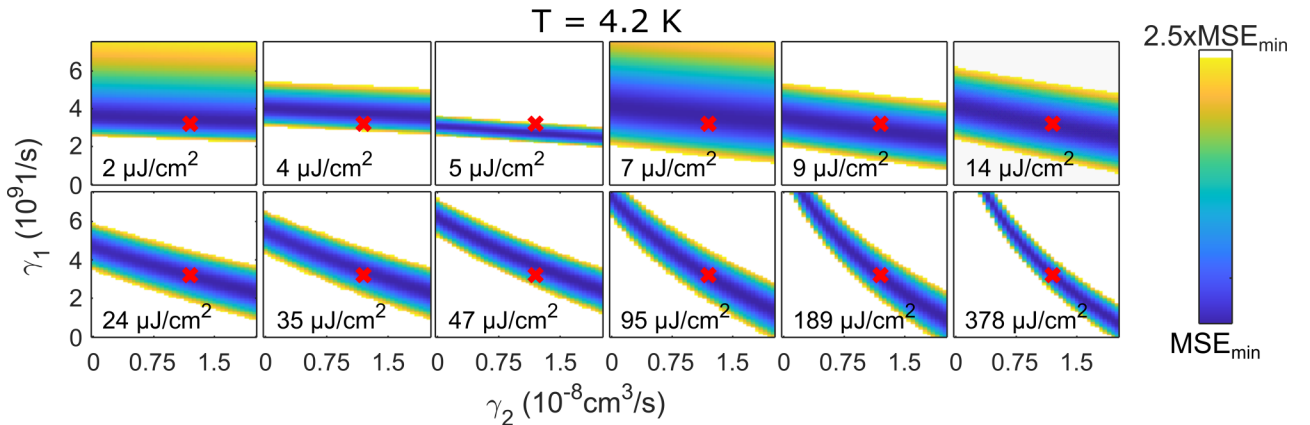


FIG. 10. MSE maps in two-dimensional parameter space of Auger (γ_2) and linear (γ_1) recombination coefficient of a complete measurement series at 4.2 K. The respective fluences are indicated in each panel. Blue-colored areas imply minima, white-colored ones an $\text{MSE} \geq 2.5 \times \text{MSE}_{\min}$. The red crosses indicate those parameter values that are simultaneously good estimates for all fluences.

with an 8-fs NIR pulse centered at a wavelength of 1200 nm and focused into a (110)-oriented ZnTe crystal with a thickness of 30 μm . The frequency response features lowpass characteristics with a (thickness-dependent [46]) cutoff frequency of approximately 30 THz. A shift in the polarization of the NIR pulse is detected with an ellipsometer setup consisting of a Wollaston prism and two balanced photodiodes. The difference signal between the two diodes is gated through a boxcar system, digitized and stored on a computer. A time trace of the THz electric field is obtained by scanning the delay between THz and NIR pulse at a constant velocity. The temporal and spatial stabilization of the laser system

allows us to constitute the time traces averaging over multiple scans.

In order to reduce noise contributions at higher frequencies, the shockwave time trace is smoothed anywhere except for a 0.5 ps time window centered at the steep increase (0.1 ps, smoothing range). This procedure is applied to all data sets analyzed in this work apart from the few-THz transient [Figs. 1(b) and 1(c)] in which there is no high-frequency signal. In addition, a Tukey window function is applied to reduce the effect of spectral leakage. The complex spectral amplitude of the waveform is calculated by performing a fast Fourier transform of the pre-processed signal.

-
- [1] J. Cabanillas-Gonzalez, G. Grancini, and G. Lanzani, *Adv. Mater.* **23**, 5468 (2011).
- [2] T. Kobayashi, *Photonics* **5**, 19 (2018).
- [3] E. Talgorn, Y. Gao, M. Aerts, L. T. Kunneman, J. M. Schins, T. J. Savenije, M. A. van Huis, H. S. J. van der Zant, A. J. Houtepen, and L. D. A. Siebbeles, *Nat. Nanotechnol.* **6**, 733 (2011).
- [4] S. Gélinas, A. Rao, A. Kumar, S. L. Smith, A. W. Chin, J. Clark, T. S. van der Poll, G. C. Bazan, and R. H. Friend, *Science* **343**, 512 (2014).
- [5] V. D'Innocenzo, G. Grancini, M. J. P. Alcocer, A. R. S. Kandada, S. D. Stranks, M. M. Lee, G. Lanzani, H. J. Snaith, and A. Petrozza, *Nat. Commun.* **5**, 3586 (2014).
- [6] F. Ceballos, Q. Cui, M. Z. Bellus, and H. Zhao, *Nanoscale* **8**, 11681 (2016).
- [7] M. A. Green, A. Ho-Baillie, and H. J. Snaith, *Nat. Photonics* **8**, 506 (2014).
- [8] X.-C. Zhang and J. Xu, *Introduction to THz Wave Photonics* (Springer, Berlin, 2010), Vol. 29.
- [9] R. Ulbricht, E. Hendry, J. Shan, T. F. Heinz, and M. Bonn, *Rev. Mod. Phys.* **83**, 543 (2011).
- [10] L. Luo, L. Men, Z. Liu, Y. Mudryk, X. Zhao, Y. Yao, J. M. Park, R. Shinar, J. Shinar, K.-M. Ho, I. E. Perakis, J. Vela, and J. Wang, *Nat. Commun.* **8**, 15565 (2017).
- [11] H. Hempel, T. J. Savenjie, M. Stolterfoht, J. Neu, M. Failla, V. C. Paingad, P. Kužel, E. J. Heilweil, J. A. Spies, M. Schleuning, J. Zhao, D. Friedrich, K. Schwarzburg, L. D. A. Siebbeles, P. Dörflinger, V. Dyakonov, R. Katoh, M. J. Hong, J. G. Labram, M. Monti, E. Butler-Caddle, J. Lloyd-Hughes, M. M. Taheri, J. B. Baxter, T. J. Magnanelli, S. Luo, J. M. Cardon, S. Ardo, and T. Unold, *Adv. Energy Mater.* **12**, 2102776 (2022).
- [12] A. Haddadi, G. Chen, R. Chevallier, A. M. Hoang, and M. Razeghi, *Appl. Phys. Lett.* **105**, 121104 (2014).
- [13] W. Lei, J. Antoszewski, and L. Faraone, *Appl. Phys. Rev.* **2**, 041303 (2015).
- [14] E. Burstein, *Phys. Rev.* **93**, 632 (1954).
- [15] T. S. Moss, *Proc. Phys. Soc. Sect. B* **67**, 775 (1954).
- [16] P. Dziawa, B. J. Kowalski, K. Dybko, R. Buczko, A. Szczerbakow, M. Szot, E. Łusakowska, T. Balasubramanian, B. M. Wojek, M. H. Berntsen, O. Tjernberg, and T. Story, *Nat. Mater.* **11**, 1023 (2012).
- [17] F. Teppe, M. Marcinkiewicz, S. S. Krishtopenko, S. Ruffenach, C. Consejo, A. M. Kadykov, W. Desrat, D. But, W. Knap, J. Ludwig, S. Moon, D. Smirnov, M. Orlita, Z. Jiang, S. V. Morozov, V. I. Gavrilenko, N. N. Mikhailov, and S. A. Dvoretzki, *Nat. Commun.* **7**, 12576 (2016).
- [18] H. Tanimura and K. Tanimura, *Phys. Rev. B* **102**, 235202 (2020).
- [19] S. Houver, L. Huber, M. Savoini, E. Abreu, and S. L. Johnson, *Opt. Express* **27**, 10854 (2019).
- [20] F. Junginger, B. Mayer, C. Schmidt, O. Schubert, S. Mährlein, A. Leitenstorfer, R. Huber, and A. Pashkin, *Phys. Rev. Lett.* **109**, 147403 (2012).
- [21] V. Dubikovskiy, D. J. Hagan, and E. W. Van Stryland, *J. Opt. Soc. Am. B* **25**, 223 (2008).
- [22] G. Li, W. Zhou, W. Zhang, G. Ma, H. Cui, Y. Gao, Z. Huang, and J. Chu, *Appl. Opt.* **57**, 9729 (2018).
- [23] J. Takayanagi, S. Kanamori, K. Suizu, M. Yamashita, T. Ouchi, S. Kasai, H. Ohtake, H. Uchida, N. Nishizawa, and K. Kawase, *Opt. Express* **16**, 12859 (2008).
- [24] A. Singh, A. Pashkin, S. Winnerl, M. Welsch, C. Beckh, P. Sulzer, A. Leitenstorfer, M. Helm, and H. Schneider, *Light Sci. Appl.* **9**, 30 (2020).
- [25] M. Knorr, J. Raab, M. Tauer, P. Merkl, D. Peller, E. Wittmann, E. Riedle, C. Lange, and R. Huber, *Opt. Lett.* **42**, 4367 (2017).
- [26] A. Grupp, A. Budweg, M. P. Fischer, J. Allerbeck, G. Soavi, A. Leitenstorfer, and D. Brida, *J. Opt.* **20**, 014005 (2018).
- [27] X. Xie, J. Dai, and X.-C. Zhang, *Phys. Rev. Lett.* **96**, 075005 (2006).
- [28] N. Karpowicz, X. Lu, and X.-C. Zhang, *J. Mod. Opt.* **56**, 1137 (2009).
- [29] V. A. Andreeva, O. G. Kosareva, N. A. Panov, D. E. Shipilo, P. M. Solyankin, M. N. Esaulkov, P. González de Alaiza Martínez, A. P. Shkurinov, V. A. Makarov, L. Bergé, and S. L. Chin, *Phys. Rev. Lett.* **116**, 063902 (2016).
- [30] J. Bühler, J. Allerbeck, G. Fitzky, D. Brida, and A. Leitenstorfer, *Optica* **5**, 821 (2018).
- [31] B. Mayer, C. Schmidt, J. Bühler, D. V. Seletskiy, D. Brida, A. Pashkin, and A. Leitenstorfer, *New J. Phys.* **16**, 063033 (2014).
- [32] A. Sell, A. Leitenstorfer, and R. Huber, *Opt. Lett.* **33**, 2767 (2008).
- [33] O. Madelung, *Semiconductors: Data Handbook* (Springer, Berlin, 2004).
- [34] A. R. Beattie, *J. Phys. C* **18**, 6501 (1985).
- [35] Y. Jiang, M. Cui, S. Li, C. Sun, Y. Huang, J. Wei, L. Zhang, M. Lv, C. Qin, Y. Liu, and M. Yuan, *Nat. Commun.* **12**, 336 (2021).
- [36] V. Chazapis, H. A. Blom, K. L. Vodopyanov, A. G. Norman, and C. C. Phillips, *Phys. Rev. B* **52**, 2516 (1995).
- [37] Y. P. Varshni, *Phys. Status Solidi* **20**, 9 (1967).

- [38] P. M. Fauchet, *Phys. Status Solidi* **110**, K11 (1982).
- [39] M. A. Zudov, A. P. Mitchell, A. H. Chin, and J. Kono, *J. Appl. Phys.* **94**, 3271 (2003).
- [40] P. Sondhaus, O. Synnergren, T. N. Hansen, S. E. Canton, H. Enquist, A. Srivastava, and J. Larsson, *Phys. Rev. B* **78**, 115202 (2008).
- [41] E. O. Kane, *J. Phys. Chem. Solids* **1**, 249 (1957).
- [42] W. Zawadzki, *Adv. Phys.* **23**, 435 (1974).
- [43] P. Y. Yu and M. Cardona, *Fundamentals of Semiconductors: Physics and Materials Properties* (Springer, Berlin, Heidelberg, 2005), Vol. 1.
- [44] E. Hecht, *Optics, 4th ed.* (Addison-Wesley Publishing Company, Boston, MA, 2001).
- [45] U. Stroth, *Plasmaphysik* (Springer, Berlin, 2018).
- [46] A. Leitenstorfer, S. Hunsche, J. Shah, M. C. Nuss, and W. H. Knox, *Appl. Phys. Lett.* **74**, 1516 (1999).